

Van Allen Belt Punctures and their Correlation with Solar Wind, Geomagnetic Activity and ULF Waves

Jayasri Joseph¹, Allison N Jaynes², Daniel N. Baker³, Xinlin Li⁴, and Shrikanth G Kanekal⁵

¹The University of Iowa

²University of Iowa

³University of Colorado Boulder

⁴U Colorado

⁵National Aeronautics and Space Administration (NASA)

November 22, 2022

Abstract

We investigate the rare events of sudden appearances of relativistic electrons (>700 keV), which are normally confined to the Van Allen belts, in the slot region. The frequency of occurrence of these events are on average 1-2 per year. To cope with the scarcity of events, in this study we examine 21 years of trapped relativistic electron fluxes available from the POES and MetOp Space Environment Monitor (SEM-2). Our statistical analysis show that these events can occur even during moderate geomagnetic activity. Occurrence of these events correlates with high speed solar winds or ICMEs depending on the phase of the solar cycle. Most importantly, we show that ULF wave activity plays a significant role in causing these events and the events could be predicted in 75% of the cases.

16 **Abstract**

17 We investigate the rare events of sudden appearances of relativistic electrons (>700 keV), which
18 are normally confined to the Van Allen belts, in the slot region. The frequency of occurrence of
19 these events are on average 1-2 per year. To cope with the scarcity of events, in this study we
20 examine 21 years of trapped relativistic electron fluxes available from the POES and MetOp
21 Space Environment Monitor (SEM-2). Our statistical analysis show that these events can occur
22 even during moderate geomagnetic activity. Occurrence of these events correlates with high
23 speed solar winds or ICMEs depending on the phase of the solar cycle. Most importantly, we
24 show that ULF wave activity plays a significant role in causing these events and the events could
25 be predicted in 75% of the cases.

26

27 **1 Introduction**

28 The Earth is protected against harsh energetic particles from space by the Van Allen radiation
29 belts – regions that contain charged particles captured by the Earth's magnetic field. The Van
30 Allen belts can be a source of highly energetic electrons (Kanekal et al., 2001) that increase and
31 decrease on varying timescales. Long-term observations of the outer radiation belt reveals that on
32 rare occasions there are punctures, which are defined in this study as a sudden enhancement of
33 relativistic (>700 keV) electron flux by greater than three orders of magnitude in the slot region
34 ($2 < L < 2.8$) within a day. These events are of importance in understanding the physics of the
35 radiation belts and the evolution of electron fluxes during geomagnetic disturbances.

36

37 Relativistic and ultra-relativistic electrons in the slot region, where important space assets
38 including GPS satellites are located, pose a natural hazard. Many studies using data from
39 numerous satellites were conducted in the past to understand and predict the energetic particle
40 appearances in the slot region. Three decades ago, the Combined Release and Radiation Effects
41 Satellite (CRRES) observed simultaneous injections of MeV protons and electrons at $2 < L < 3$
42 after a solar flare event as reported by Blake et al. (1992). This event created a third radiation
43 belt due to the interplanetary shock impact and was reproduced in a simulation by Li et al.
44 (1993). A model to forecast the relativistic electron fluxes in real time inside geosynchronous
45 orbit and down to $L = 2.5$ in extreme storm events was also developed by Li et al. (2009). Zhao
46 and Li (2013) analyzed ten years of SAMPEX 2–6 MeV electron flux data and found 23
47 injection events during which the electron flux at $L = 2.5$ increased by at least one order of
48 magnitude. They also noted a correlation of injection events with IMF magnitude, IMF Bz, solar
49 wind electric field, and solar wind speed. However, there are some disagreements about the
50 detection of electrons with energies above 1 MeV in the slot region by the SAMPEX instrument
51 (Selesnick, 2015). As electron flux enhancement is a prerequisite for the appearance of electrons
52 in the slot region, many studies focused on electron activities inside the radiation belt. Kanekal
53 (2006) examined the SAMPEX and Polar data and showed that the electron energization in the
54 radiation belt could be either due to radial diffusion or wave-particle interactions. He also
55 showed a correlation between the energization processes and the phases of the solar cycle.
56 Rodger et al. (2010) studied 10 years of measurements of trapped and precipitating electrons
57 from the POES Satellites and showed that the relativistic (>800 keV) electron enhancement in
58 the belt lags by approximately one week relative to the low energy (~ 30 keV) electron
59 enhancement. Many observations of the outer radiation belt indicated a nominal energy

60 dependent barrier isolating the slot region from the belt. The Relativistic Electron Proton
61 Telescope (REPT) instrument onboard the Van Allen Probes mission detected a very sharp inner
62 boundary of the outer radiation belt for the ultra-relativistic electrons (>2 MeV) at $L=2.8$, which
63 was reported by Baker et al. (2014) and referred to as ‘impenetrable barrier’. This barrier
64 becomes semi-rigid for low-energy electrons and a rigidity profile of the barrier was recorded by
65 Turner et al. (2016). They studied electron fluxes of the radiation belts from Van Allen Probes
66 data during 2012–2014 and found that sudden particle enhancements (SPELLS) at $L < 2.8$ are
67 common for low-energy electrons but decreases exponentially with increasing electron energies
68 greater than 100 keV. Relativistic punctures, which involve electrons with energies >700 keV,
69 are relatively rare phenomena.

70
71 Along with the observation and cataloging of the enhancements of the relativistic and ultra-
72 relativistic electrons in the slot region, various studies were conducted to determine the
73 underlying cause of the sudden appearance of these electrons in the radiation belt. Baker et al.
74 (1998) and Rostoker et al. (1998) each suggested that a relativistic electron flux enhancement
75 needs both seed electron population of energy 100 – 200 keV and powerful occurrence of ULF
76 waves in the PC 4 –5 frequency range. Rostoker et al. (1998) also noted that ULF waves tend to
77 accompany high speed solar wind streams. Liu et al. (1999) proved this observation of
78 acceleration of electrons by large scale ULF wave theoretically. O’Brien et al. (2001) performed
79 an extensive statistical analysis of energetic electron enhancements using data from GOES and
80 LANL. Their superposed analysis revealed that along with the solar wind velocity, the ULF
81 power recorded by ground stations are an indicator of energetic electron enhancements. A data
82 base of ULF wave activity indices, which were derived from the world-wide array of magnetic
83 data from the ground stations and from the three-component magnetometer data from the
84 geostationary GOES spacecrafts, were cataloged by Philipenko et al. (2017).

85
86 As puncture events are a relatively rare phenomena, data samples over many years, preferably
87 from a single instrument, are needed to carry out a meaningful statistical analysis and determine
88 possible prediction strategies. Moreover, to see any correlation of these events with solar cycle
89 variations, observations spanning at least a couple of solar cycles is required. Here we use the
90 Space Environment Monitor (SEM-2) instruments on the Polar Orbiting POES and MetOp
91 satellites to obtain a continuous data set for puncture events spanning the last 21 years. SEM-2
92 instruments are not designed to measure relativistic electrons, although we can utilize proton
93 channels contaminated by high-energy electrons. We trade off the inaccuracy in the energy range
94 measurement for the long periods of continuous observations. Low altitude polar orbits also have
95 the added advantage of sampling the belts frequently and recording events with a greater
96 temporal accuracy than equatorially orbiting satellites.

97
98
99 In this work, we firstly identify the puncture events and perform a statistical analysis involving
100 various solar wind parameters and indices during different phases of solar cycles. We show that
101 the roles played by solar wind to cause a puncture is different during the rising and falling phases
102 of the solar cycles. Secondly, we analyzed the correlation of puncture events with the ULF wave
103 activity. We show that 75% of the observed puncture events over the last 21 years match with
104 predicted events using an algorithm based on the ULF wave activity indices.

105

106

107 **2 Instrument**

108 In this study we use particle measurements by the SEM-2 instrument package onboard the POES
 109 and MetOp satellites. These satellites traverse Sun-synchronous orbits at an altitude of ~800–
 110 850 km. SEM-2 is a multichannel, charged-particle spectrometer that measures the population of
 111 electrons and protons in the Earth's radiation belts and is used to observe particle fluxes
 112 variations resulting from solar and extrasolar activity. There are two orthogonal channels that
 113 measure electron fluxes at 0° and 90°. The 0° measurements come from detectors that are
 114 mounted on the three-axis stabilized platform pointing outward and parallel to the Earth-center-
 115 to-satellite radial vector. The 90° measurements come from the detectors that are mounted
 116 approximately perpendicular to the 0° detectors. Table 1 lists the detector channels that respond
 117 to electrons of various energy ranges. From Table 1, it can be noted that the P6-detector, which is
 118 designed to measure >6.9 MeV protons, also responds to electrons, with energies starting from
 119 700 keV. In this work, we use the P6-90 channel as a proxy for the trapped relativistic electron
 120 measurements of the Van Allen belt.

121

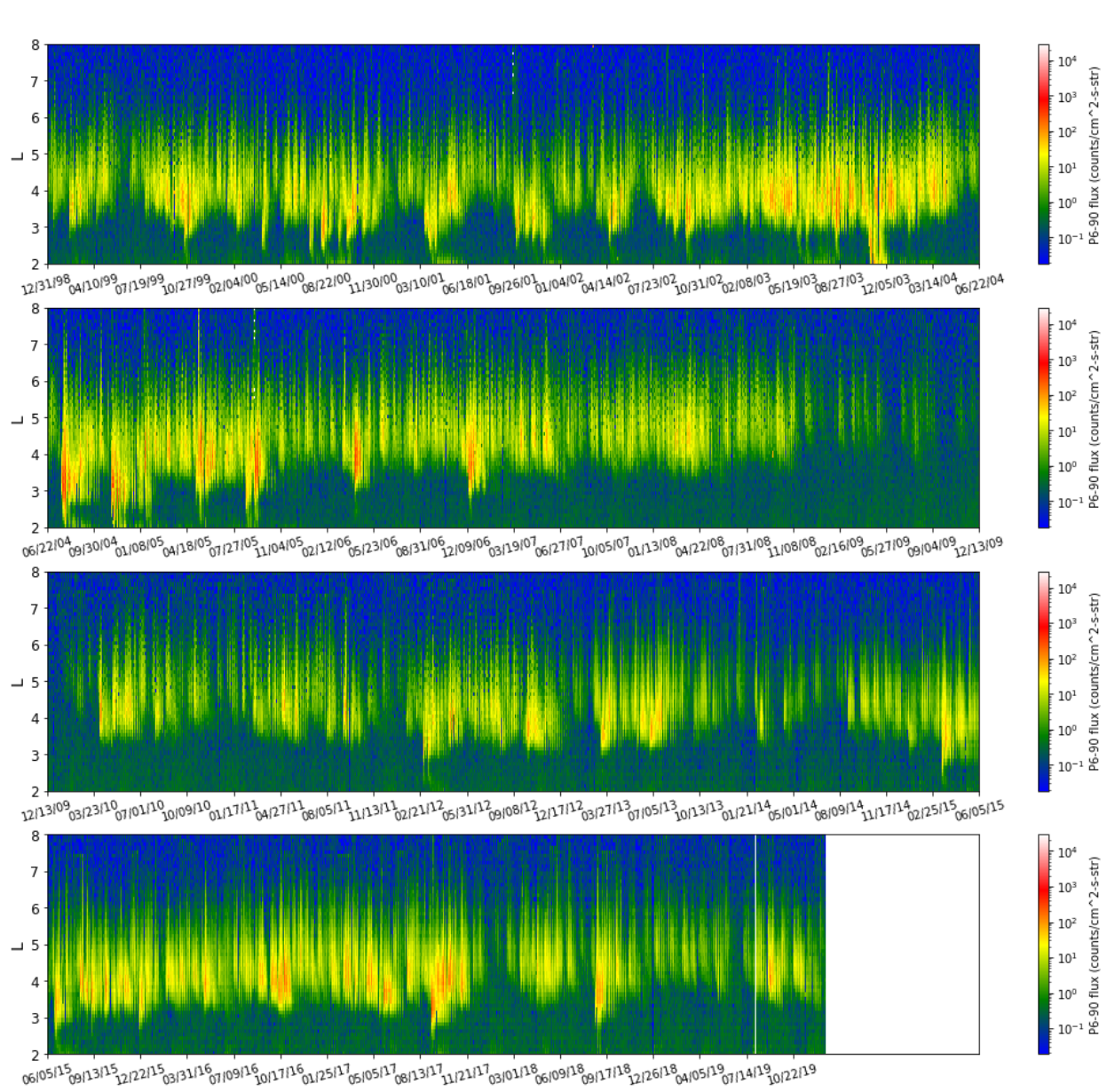
122 Table 1. List of SEM-2 energy channels that respond to electrons

Particle - Data Channel	Energy Range	Contaminants
Electron – e1	30 keV to 2500 keV	Proton - 210 keV to 2700 keV
Electron – e2	100 keV to 2500 keV	Proton - 280 keV to 2700 keV
Electron – e3	300 keV to 2500 keV	Proton - 440 keV to 2700 keV
Proton – p6	>6900 keV	Electron – greater than 700 keV

123

124 **3 Data**

125 We use SEM-2 data from two polar orbiting satellites over 21 years, from 1999 to 2019. The
 126 period from the 1st January, 1999 to the 31st December, 2012 and from the 1st January, 2013 to
 127 the 31st December, 2019 are covered by the NOAA-15 and the Metop-2 satellite, respectively.
 128 NOAA-15 data is available at a 16-second resolution, and Metop-2 data is available at a two-
 129 second resolution. The time series representing the relativistic electron flux, namely the p6-90
 130 channel, along with the corresponding L-shell, namely the LGRF parameter, were extracted.
 131 Time periods of true solar proton events (SPE) have been excluded by using solar proton activity
 132 indications from the P7 omnidirectional detector. This left us with only times during which there
 133 are relativistic electron counts in the P6 data channel. Figure 1 shows the electron flux variation
 134 with L-shell over past 21 years.



135

136

137

Figure 1. P6-90 electron flux variation with time and L-shell for last 21 years.

138

Supplementary measurements of one-hour averaged values of solar wind speed, dynamic pressure, electric field and interplanetary magnetic field and geomagnetic indices Dst, Kp and AE were obtained from the NASA OMNI database. ULF indices were obtained from the catalog at <http://ulf.gcras.ru/archive.html>.

140

141

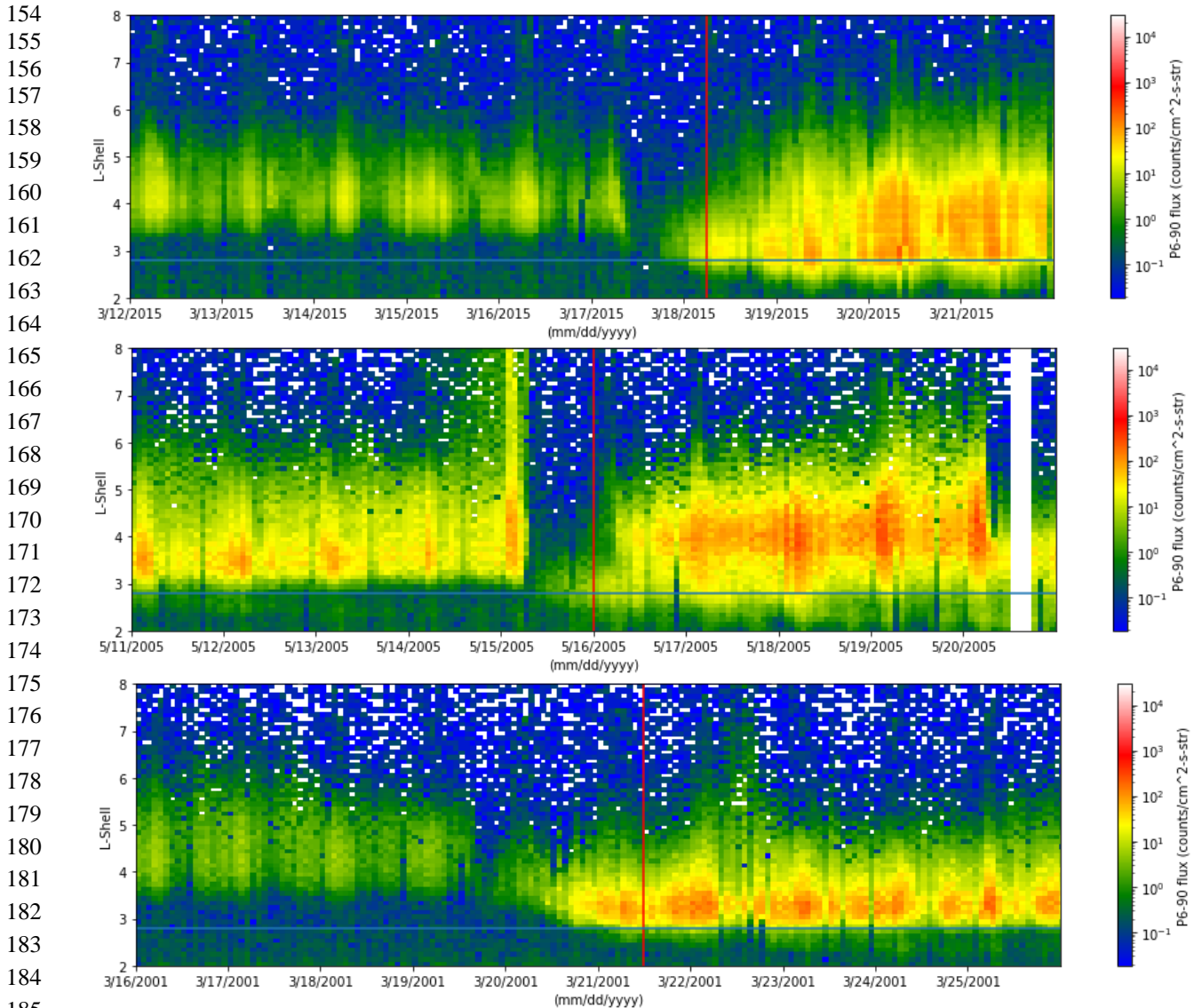
142

143 4 Events

144 Puncture events are identified from the time series of the electron flux in the slot region. The
 145 event selection process is described in section 4.1. As events could arise from various physical
 146 conditions, we categorize them in section 4.2 before carrying out statistical analysis.

147 4.1 Event selection

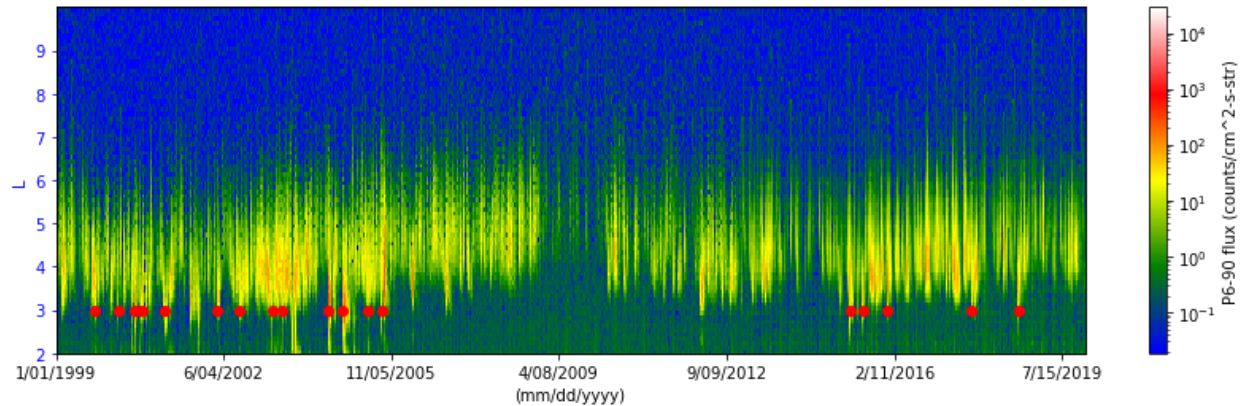
148 An algorithmic approach is employed for event selection to allow for the varying nature of the
 149 puncture events. Our detection algorithm calculates a running average of the electron flux in the
 150 region between $2 < L < 2.8$. An event is considered if there is a positive step change in the electron
 151 flux by three orders of magnitude. A minimum gap of three days between two events is set to
 152 avoid multiple detection. All events detected during an SPE are ignored. A few examples of
 153 events are shown in Figure 2.



186 Figure 2. Examples of event detection (red vertical lines). SPE regions are blanked out (white
 187 vertical stripes).

188

189 The algorithm detected 45 events. Events occurring either overlapping SPE events or within a
 190 few hours to SPE events were manually removed. We selected 19 events, which involved only
 191 relativistic electrons, for our analysis as shown in Figure 3. It must be noted that some of the
 192 puncture events, which were discarded to avoid data ambiguity, could have been true punctures.
 193



194

195 Figure 3. The relativistic electron flux density over 21 years. Selected puncture events are
 196 denoted by red dots.

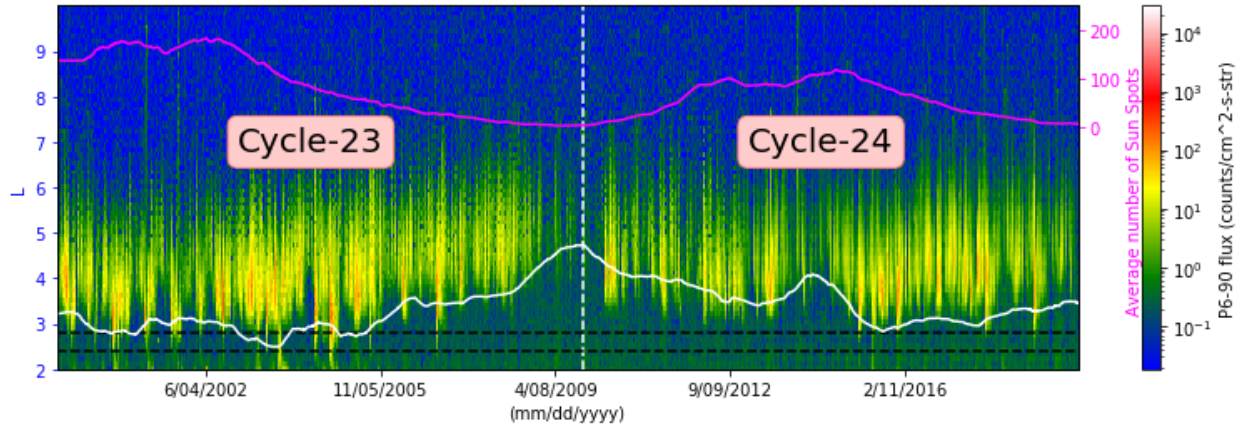
197

198 4.2 Event category

199 A sudden flux increase of relativistic electrons in the slot region is a necessary condition for a
 200 puncture event. Radiation belt electron flux variations occur during solar storms, which are
 201 caused by either high-speed solar wind-streams (HSSWS) or interplanetary coronal mass
 202 ejections (ICMEs) (Friedel et al., 2002). While ICMEs are the main source of geomagnetic
 203 storms during the ascending phase of the solar cycle and solar maximum, high-speed (>500
 204 km/s) solar wind-streams play a significant role in the declining phase and solar minimum
 205 (Richardson et al., 2000). To reflect the differences in the underlying mechanisms that cause
 206 electron puncture events, we break down our data into two categories, which correspond to the
 207 ascending and the descending phases of the solar cycle. Average sunspot number is used to
 208 determine the phase of the solar cycle.

209 The condition for breaching the barrier may also depend on the position of the belt's lower
 210 boundary. During solar cycle 23 the radiation belt was closer to the earth compared to solar cycle
 211 24 as shown in figure 4.

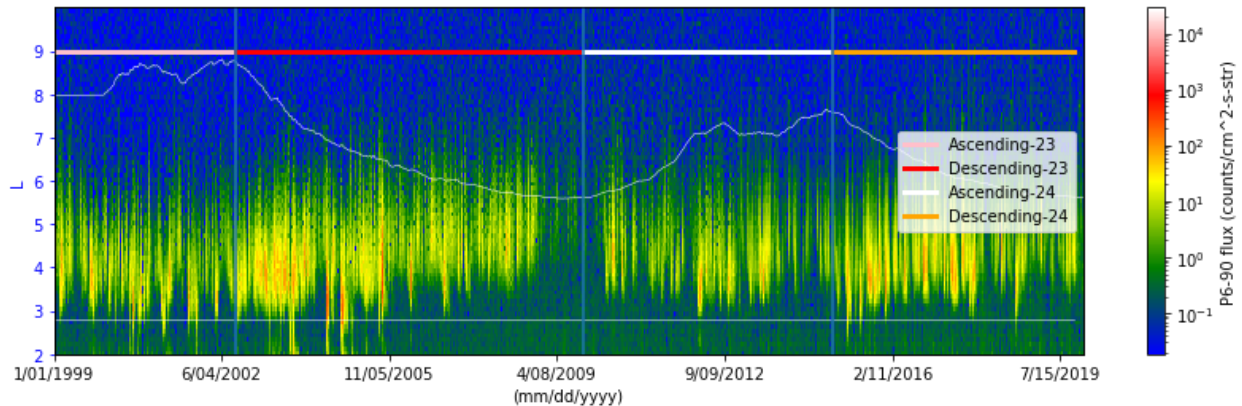
212



213
 214 Figure 4. Long-term variation of the lower boundary of the outer radiation belt (white trace) with
 215 averaged sunspot numbers (magenta trace).

216
 217 To account for this cycle-to-cycle variation, we further divide the data into subcategories as
 218 ascending-23, descending-23, ascending-24 and descending-24 for solar cycles 23 and 24, as
 219 shown in Figure 5. Both ascending-23 and descending-23 categories have seven suitable events
 220 each and the descending-24 category has five events. There are no unambiguous puncture events
 221 in the ascending-24 category.

222



223
 224 Figure 5. Solar cycle zones to categorize events. Top white trace is the averaged sunspot
 225 numbers.

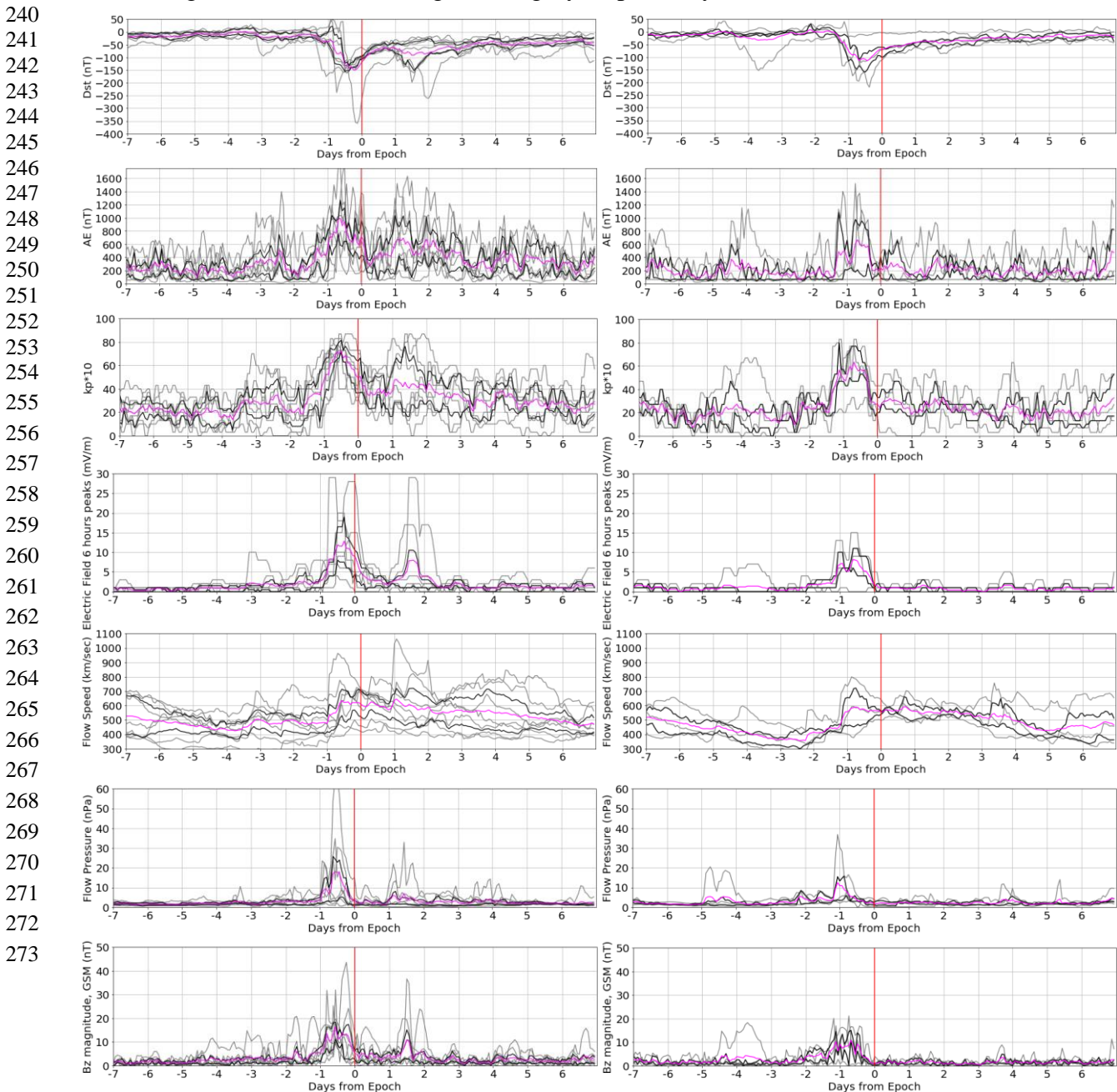
226

227 **5 Analysis**

228 In this study, we conduct a two-fold analysis of the puncture events. Firstly, we look at various
 229 solar indices and solar/magnetospheric parameters around the events. Results of the statistical
 230 analysis are presented in section 5.1. Secondly, we examine the ULF wave activity over the
 231 study period of 21 years. We then suggest an algorithm that determines the occurrence of
 232 punctures, based on this ULF activity. A description of the algorithm and the results are
 233 presented in section 5.2.

234 **5.1 Superposed Epoch Analysis**

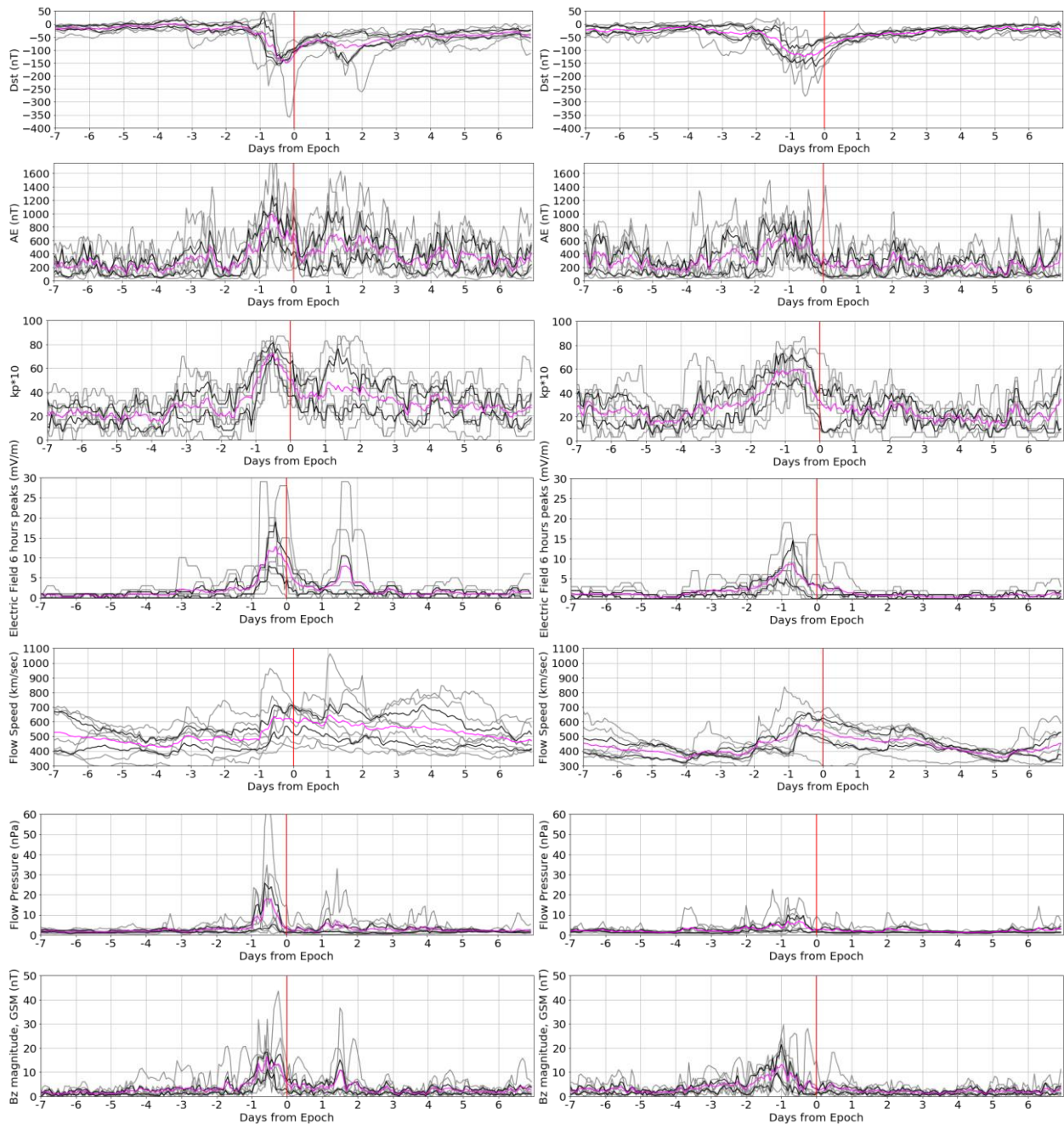
235 In this analysis, the puncture event time, which is determined by the event selection algorithm
 236 (section 4.1), is defined as the 0-epoch. A window of 14 days centered around the event is used
 237 in the analysis. Figure 6 and Figure 7 show the superposed epoch analysis of various solar wind
 238 parameters and indices. The left panels and the right panels of Figure 6 are the results during the
 239 descending-23 and the descending-24 category respectively.



274
 275
 276
 277
 278
 279
 280
 281
 282
 283
 284
 285
 286
 287
 288
 289
 290
 291
 292
 293
 294
 295
 296
 297
 298
 299
 300
 301
 302
 303
 304
 305
 306
 307
 308
 309
 310
 311
 312
 313
 314
 315
 316
 317
 318
 319
 320
 321

Figure 6. Superposed epoch analysis - left panel and right panel represent solar parameters in descending-23 and descending-24 category respectively. Solar parameters variation (gray lines), mean value (magenta lines), 25th and 75th quartile values (black lines) around the puncture events.

The superposed epoch analysis of descending-23 and ascending-23 categories are shown in Figure 7.



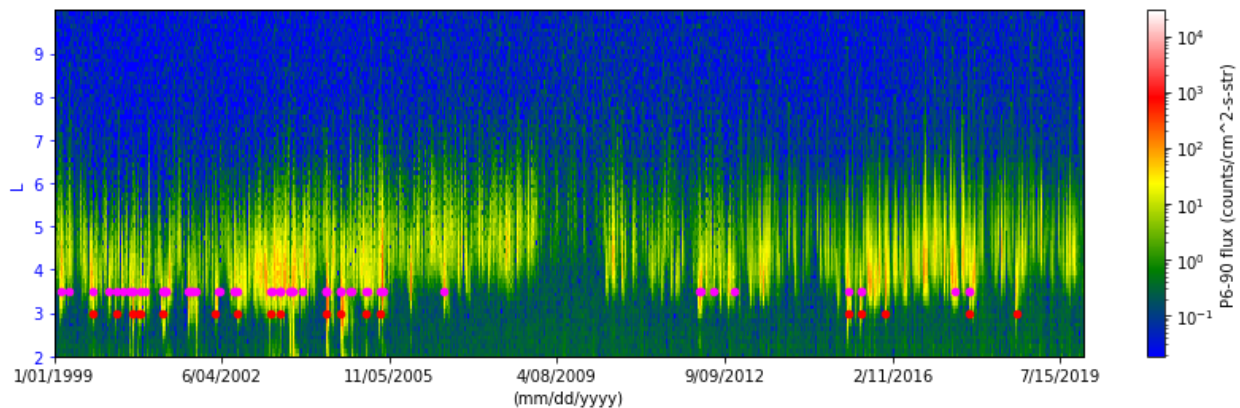
322
323
324
325
326
327

Figure 7. Superposed epoch analysis - left panel and right panel represent solar parameters in descending-23 and ascending-23 category respectively. Solar parameters variation (gray lines), mean value (magenta lines), 25th and 75th quartile values (black lines) around the puncture events.

328
329
330
331
332
333
334
335
336
337
338
339
340
341
342
343
344
345

5.2 ULF Wave Analysis and Puncture Prediction

In this analysis we estimate the enhancement of the energetic electrons in the slot region from the ULF wave activity. Our algorithm uses the ULF indices from the database at <http://ulf.gcras.ru/archive.html> as a proxy for the strength of ULF signals. From the database we extract two indices, namely the ULF-ground and the ULF-goes. ULF-ground was obtained from the world-wide array of magnetic stations in the Northern hemisphere. ULF-goes was derived from the magnetometers onboard GOES spacecraft. Our prediction algorithm scans the hourly ULF-ground index to identify large disturbances (>200 nT) at very low L-shell. Then the algorithm searches for corresponding disturbances at the geostationary orbit using the ULF-goes index, which reflects the ULF activity at $L=6.6$. At the geostationary orbit a magnetic disturbance greater than 10 nT is considered significant. We intuit ULF activity in the slot region if a large ULF event occurs simultaneously at the ULF-ground and ULF-goes. The strength of the ULF waves at the geostationary orbit and on the ground, which surround the slot region, is used to predict the puncture events. Figure 8 shows the predicted puncture events in magenta and the identified puncture events in red dots. It should be noted that we discarded many potential puncture events to avoid ambiguity in the input data.



346
347
348
349
350
351
352
353
354
355
356

Figure 8. The relativistic electron flux density over 21 years. Puncture events are shown as red dots and predicted events are shown as magenta dots.

6 Discussion and Conclusions

In Figure 6, the solar/magnetospheric parameters are consistently smaller in the right panel representing the descending-24 compared to the left panel representing descending-23. This indicates that the puncture events have no direct correlation with the strength of the geomagnetic activity. Punctures can occur even during a relatively weak solar cycle.

357 From the fifth row in Figure 7 it can be noted that in the descending-23 category (left panel), the
358 solar wind speed rises over a day and then declines more slowly over several days as compared
359 to the ascending-23 category (right panel). It can also be noted that in the left panels all
360 geomagnetic activities persist for many days as oppose to the right panels where the disturbances
361 are likely caused by ICME. ICME events are more transient, driving high geomagnetic activity
362 for typically only 1–2 days (Richardson et al., 2000).

363

364 Approximately 75% of the puncture events could be predicted by our algorithm (Figure 8). The
365 ULF indices database that we used did not include the magnetic stations located in the southern
366 hemisphere. Moreover, we can investigate additional puncture events that were predicted by our
367 algorithm, but were not included as punctures in this study, possibly due to our event detection
368 limitations. All the punctures that occurred during or adjacent to SPE were ignored to avoid the
369 proton contamination in the detector. Careful study of individual events may be necessary to
370 consider those that were left out of this statistical picture.

371

372 Energetic electrons can breach the energy-dependent barrier and transit the slot region on
373 occasion, during both ICME and HSS solar driving events. There is no correlation of these
374 puncture events with storm strength or overall geomagnetic activity, however, there exists a
375 strong correlation with ULF wave activity. This study shows the importance of ULF waves in
376 energetic electron enhancements that cause punctures, and, in most cases, it is possible to have a
377 warning.

378

379

380 **Acknowledgments and Data**

381 The primary author wishes to acknowledge the use of funds from NASA's Van Allen Probes
382 ECT project, through JHU/APL contract 967399 under prime NASA contract NAS5-01072.
383 NOAA-15 data is available from

384 <https://satdat.ngdc.noaa.gov/sem/poes/data/processed/swpc/uncorrected/avg/cdf/>

385 (<http://mag.gmu.edu/ftp/POES/n15/>). Metop-2 data is available from

386 https://spdf.gsfc.nasa.gov/pub/data/noaa/metop2/sem2_fluxes-2sec/. Solar wind OMNI data is

387 available from <https://omniweb.gsfc.nasa.gov/form/dx1.html>. ULF wave activity indices are

388 available from ULF wave index database - ESDB repository, GC RAS, Moscow,

389 <https://doi.org/10.2205/ULF-index> (<http://ulf.gcras.ru/archive.html>).

390 **References**

391 Baker, D. N., X. Li, J. B. Blake, and S. Kanekal (1998), Strong electron acceleration in the
392 Earth's magnetosphere, *Adv. Space Res.*, 21, 609, doi:10.1016/S0273-1177(97)00970-8.

- 393 Baker, D. N., et al. (2014), An impenetrable barrier to ultrarelativistic electrons in the Van Allen
394 radiation belts, *Nature*, 515, 531– 534, doi:10.1038/nature13956.
- 395 Blake, J. B., W. A. Kolasinski, R. W. Fillius, and E. G. Mullen (1992), Injection of electrons and
396 protons with energies of tens of MeV into L less than 3 on 24 March 1991, *Geophys. Res. Lett.*,
397 19, 821–824, doi:10.1029/92GL00624
- 398 Friedel, R. H. W., G. D. Reeves, and T. Obara (2002), Relativistic electron dynamics in the inner
399 magnetosphere—A review, *J. Atmos. Sol. Terr. Phys.*, 64, 265, doi:10.1016/S1364-
400 6826(01)00088-8.
- 401
- 402 Kanekal, S. G., Baker, D. N., & Blake, J. B. (2001), Multisatellite measurements of relativistic
403 electrons: *Global coherence*, *Journal of Geophysical Research: Space Physics*, 106(A12),
404 29721-29732, doi: 10.1029/2001JA000070.
- 405
- 406 Kanekal, S. G. (2006), A review of recent observations of relativistic electron energization in the
407 Earth's outer Van Allen radiation belt, *Proceedings of the ILWS Workshop on Solar Influence on*
408 *the Heliosphere and Earth's Environment*, Goa, India, Quest Publications, Goa
- 409
- 410 Li, X., et al. (1993), Simulation of the prompt energization and transport of radiation belt
411 particles during the March 24, 1991 SSC, *Geophysical Research Letters*, 20, Issue 22,
412 doi:10.1029/93GL02701.
- 413
- 414 Li, X., A. B. Barker, D. N. Baker, W. C. Tu, T. E. Sarris, R. S. Selesnick, R. Friedel, and C. Shen
415 (2009), Modeling the deep penetration of outer belt electrons during the “Halloween” magnetic
416 storm in 2003, *Space Weather*, 7, S02004, doi:10.1029/ 2008SW000418.
- 417
- 418 Liu, W. W., G. Rostoker, D. N. Baker (1999), Internal acceleration of relativistic electrons by
419 large-amplitude ULF pulsations, *J. Geophys. Res. Space Physics*, 104, Issue A8,
420 doi:10.1029/1999JA900168.
- 421
- 422 O'Brien, T. P., et al. (2001), Which magnetic storms produce relativistic electrons at
423 geosynchronous orbit?, *J. Geophys. Res.*, 106, NO. A8, 15,533-15,54,
424 doi:10.1029/2001JA000052.
- 425
- 426 Pilipenko, V., O. Kozyreva, M. Engebretson (2017), ULF wave index database, *ESDB*
427 *repository*, *GC RAS*, Moscow, doi:10.2205/ULF-index.
- 428
- 429 Richardson, I. G., E. W. Cliver, and H. V. Cane (2000), Sources of geomagnetic activity over the
430 solar cycle: Relative importance of CMEs, high-speed streams, and slow solar wind, *J. Geophys.*
431 *Res.*, 105, 18,203, doi:10.1029/1999JA000400.
- 432
- 433 Rodger, C. J., M. A. Clilverd, J. C. Green, and M. M. Lam (2010), Use of POES SEM-2
434 observations to examine radiation belt dynamics and energetic electron precipitation into the
435 atmosphere, *J. Geophys. Res.*, 115, A04202, doi:10.1029/2008JA014023.
- 436

437 Rostoker, G., S. Skone, and D. N. Baker (1998), On the origin of relativistic electrons in the
438 magnetosphere, *Geophys. Res. Lett.*, 25, 3701-3704, doi:10.1029/98GL02801.
439

440 Selesnick, R. S. (2015), Measurement of inner radiation belt electrons with kinetic energy above
441 1 MeV, *J. Geophys. Res. Space Physics*, 120, 8339–8349, doi:10.1002/2015JA021387.
442

443 Turner, D. L., et al. (2017), Investigating the source of near-relativistic and relativistic electrons
444 in Earth’s inner radiation belt, *J. Geophys. Res. Space Physics*, 122, 695–710, doi:10.1002/
445 2016JA023600.
446

447 Zhao, H., and X. Li (2013), Inward shift of outer radiation belt electrons as a function of Dst
448 index and the influence of the solar wind on electron injections into the slot region, *J. Geophys.*
449 *Res. Space Physics*, 118, 756–764, doi:10.1029/2012JA018179.
450
451
452
453